Geophys. J. Int. (1998) **135,** 585–594

Seismic reflection and transmission coefficients of a self-similar interface

Kees Wapenaar

Centre for Technical Geoscience, Laboratory of Seismics and Acoustics, Delft University of Technology, PO Box 5046, 2600 GA *Delft, the Netherlands. E-mail: C.P.A.Wapenaar@CTG.TUDelft.NL*

Accepted 1998 July 14. Received 1998 July 10; in original form 1996 November 11

SUMMARY

The derivation of seismic reflection and transmission coefficients is generally based on the assumption that the medium parameters behave as step functions of depth, at least in a finite region around the interface. However, outliers observed in well logs generally behave quite differently from step functions. In this paper we represent an interface by a self-similar singularity, embedded between two homogeneous half-spaces, and we derive its frequency-dependent normal-incidence reflection and transmission coefficients. For $\omega \to 0$ the expressions for the coefficients reduce to those for a discrete boundary between two homogeneous half-spaces; for $\omega \to \infty$ they become frequency-independent. These asymptotic expressions have a relatively simple form and depend on the singularity exponent α.

The exact as well as the asymptotic expressions are used to evaluate the time-domain reflection and transmission responses of a self-similar interface. Finally, we use a numerical method to model the response of a smoothed version of a self-similar interface (note that the velocity of a smoothed singularity remains finite). It turns out that smoothing has hardly any effect on the response, provided that the smoothing does not affect the scales corresponding to the seismic frequency range.

Key words: numerical methods, seismic reflection, transmission.

INTRODUCTION

The derivation of seismic reflection and transmission coefficients is generally based on a model consisting of two homogeneous layers, separated by a horizontal interface. This implies that the medium parameters behave as step functions of the depth coordinate z, at least in a finite region around the interface. However, it appears that in well logs the main outliers behave quite differently from step-functions (Fig. 1). Herrmann (1997) investigated the character of these outliers by applying the multiscale singularity detection procedure, as proposed by Mallat & Hwang (1992), to well logs. In general the local scaling behaviour of these outliers deviates significantly from that of step functions (Herrmann & Staal 1996).

In the following we parametrize an outlier of the *P*-wave velocity by the singular function

$$c(z) = \begin{cases} c_1 |z/z_1|^{\alpha} & \text{for } z < 0, \\ c_2 |z/z_2|^{\alpha} & \text{for } z > 0. \end{cases} \tag{1}$$

For convenience the singular point has been chosen at $z = 0$. For $\alpha = 0$ this function reduces to a step function. For arbitrary α this function is *self-similar*, according to $c(\beta z) = \beta^{\alpha} c(z)$, for $\beta > 0$. For the parameters α, c_n and z_n listed in Table 1, the function $c(z)$ as defined by eq. (1) is shown in Fig. 2(a). We applied a multiscale analysis to this function, following the method of Mallat & Hwang (1992). Fig. 2(b) shows the continuous wavelet transform $\check{c}(\sigma, z)$ of this function, obtained by convolving $c(z)$ with scaled versions of an analysing wavelet $(1/\sigma)\psi(z/\sigma)$ (this wavelet will be discussed in more detail in a later section). The different traces in Fig. 2(b) correspond to different scales σ. Taking the modulus of the data in Fig. 2(b) and connecting the local maxima from trace to trace yields the modulus maxima line (Fig. 2c). Fig. 2(d) shows the amplitudes measured along this line, in a log–log plot. The slope of this amplitude-versus-scale (AVS) graph corresponds to the

Table 1. Parameter values used in the examples in this paper.

	$z < 0$ $(n = 1)$	$z > 0$ $(n = 2)$
α	-0.4	-0.4
c_n (m s^{-1})	800	1200
z_n (m)	-5	5

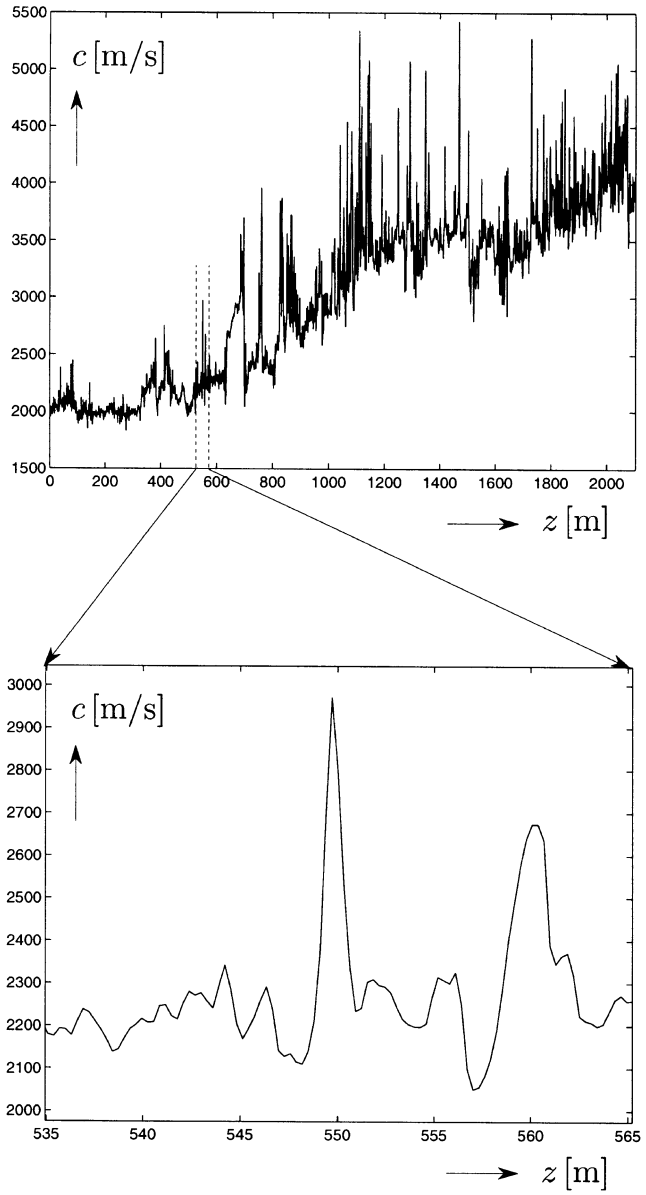

Figure 1. Well log of *P*-wave velocity $c(z)$. We parametrize outliers like the one at $z = 550$ m by self-similar functions.

singularity exponent $\alpha = -0.4$ of the self-similar function in Fig. 2(a) (Mallat & Hwang 1992). For a step function, the slope of the AVS curve would be zero.

The AVS behaviour in Fig. 2d is similar to that of several outliers in real well logs, as analysed by Herrmann (1997), with the restriction that for real well logs the AVS curves reveal a 'constant-slope' behaviour only for a finite range of scales. For small as well as large scales these AVS curves may deviate significantly from the constant-slope behaviour. Moreover, in real well logs the velocity will not go to infinity. To comply with this, we modify the parametrization of the singularity. First, consider the situation in which a self-similar singularity is embedded between two homogeneous half-spaces. A multiscale analysis of such an embedded singularity is shown in Fig. 3. The singular function in Fig. 3(a) is defined in the region $z_1 < z < z_2$ with the parameters of Table 1; the velocities of the embedding half-spaces are $c_1 = 800$ m s^{-1} and $c_2 = 1200$ m s^{-1}, so that $c(z)$ is continuous at z_1 and z_2. As $\sigma \to 0$ the AVS curve in Fig. 3(d) approaches that in Fig. 2(d). In this limit the embedding half-spaces have no effect on the scaling behaviour. As $\sigma \to \infty$ the AVS curve is nearly constant (as for a step function), which implies that in this limit the scaling behaviour is fully determined by the embedding half-spaces. Next, Fig. 4 shows a multiscale analysis of a smoothed version of the embedded singularity of Fig. 3(a). Note that the velocity in Fig. 4(a) is finite. As $\sigma \to 0$ the AVS curve in Fig. 4d deviates significantly from those in Figs 2(d) and 3(d). As $\sigma \to \infty$ the AVS curve approaches that in Fig. 3(d). For the intermediate scale range the AVS curve reveals again a constant-slope behaviour, comparable to that of several outliers in real well logs. Hence, the embedded self-similar singularity and its smoothed version are suitable (but not unique) representations of outliers in real well logs.

The aim of this paper is to analyse the seismic reflection and transmission responses of scale-dependent interfaces that resemble outliers in real well logs (in the sense that their AVS curves reveal a constant-slope behaviour over a specific range of scales). Exact expressions will be derived for the normal-incidence reflection and transmission coefficients of a self-similar singularity, embedded between two homogeneous half-spaces (as in Fig. 3a). Using these coefficients, the time-domain reflection and transmission responses of this type of scale-dependent interface will be evaluated. The responses of a smoothed version of this type of interface (as in Fig. 4a) will

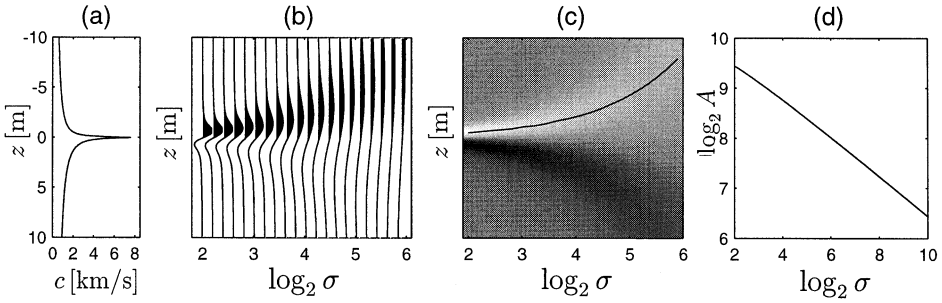

Figure 2. (a) Self-similar velocity function, described by eq. (1), with α, c_n and z_n listed in Table 1. (b) Continuous wavelet transform of the velocity function in (a). (c) Modulus maxima line, obtained from (b). (d) Amplitude-versus-scale (AVS) curve, measured along the modulus maxima line in (c). The slope ($\alpha = -0.4$) corresponds to the singularity exponent of the function in (a).

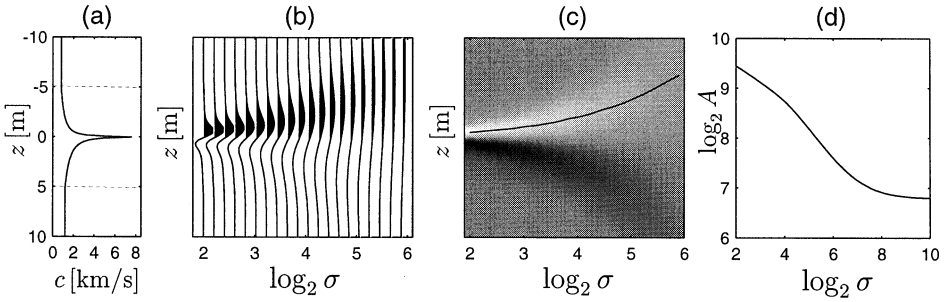

Figure 3. (a) Self-similar velocity function of Fig. 2(a), embedded between two homogeneous half-spaces $z \le z_1 = -5$ m and $z \ge z_2 = 5$ m, with velocities $c_1 = 800$ m s^{-1} and $c_2 = 1200$ m s^{-1}, respectively. (b) Continuous wavelet transform of the velocity function in (a). (c) Modulus maxima line, obtained from (b). (d) AVS curve, measured along the modulus maxima line in (c). For small σ the slope is constant and again given by $\alpha = -0.4$; for large σ the slope approaches zero, as for a step function.

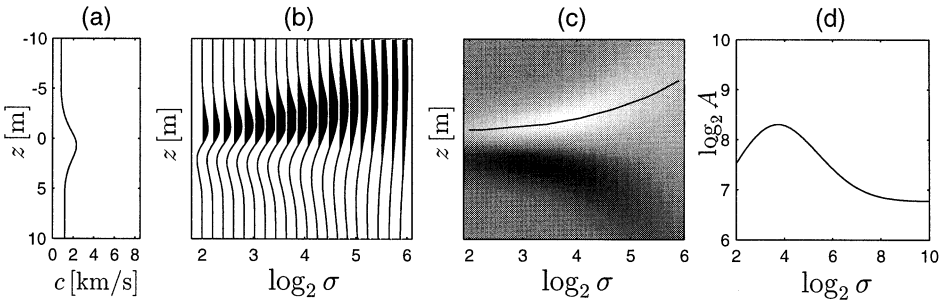

Figure 4. (a) Smoothed version of the embedded singularity of Fig. 3(a). (b) Continuous wavelet transform of the velocity function in (a). (c) Modulus maxima line, obtained from (b). (d) AVS curve, measured along the modulus maxima line in (c). This curve reveals a constant-slope behaviour ($\alpha \approx -0.4$) only for a finite scale range ($\log_2 \sigma = 4$ to $\log_2 \sigma = 8$).

be evaluated numerically. The behaviour of the band-limited seismic responses will be related to the scale behaviour of the interfaces.

BASIC SOLUTIONS

In this section we solve the one-dimensional wave equation for the velocity function $c(z) = c_1 |z/z_1|^\alpha$ for all $z \neq 0$. In the following sections the solutions will be used for an embedded self-similar interface. Given this $c(z)$ and a constant mass density, the one-dimensional wave equation (in the space–frequency domain) for the acoustic pressure $P(z, \omega)$ is

$$\frac{\partial^2 P}{\partial z^2} + \left(\frac{\omega}{c_1}\right)^2 \left|\frac{z}{z_1}\right|^{-2\alpha} P = 0, \qquad \text{for } z \neq 0, \tag{2}$$

where ω is the angular frequency (throughout this paper we only consider positive ω). By making the substitution

$$P(z, \omega) = \zeta^\nu Q(\zeta), \tag{3}$$

with

$$\zeta = \chi \left|\frac{z}{z_1}\right|^{1/2\nu}, \tag{4}$$

$$\chi = \frac{2\nu\omega|z_1|}{c_1} \tag{5}$$

and

$$\nu = \frac{1}{2 - 2\alpha}, \tag{6}$$

the wave equation (2) is transformed into

$$\zeta^2 \frac{\partial^2 Q}{\partial \zeta^2} + \zeta \frac{\partial Q}{\partial \zeta} + (\zeta^2 - \nu^2) Q = 0, \quad \text{for} \quad \zeta \neq 0, \tag{7}$$

which is the Bessel equation for $Q(\zeta)$, with real-valued ζ and ν. The solution of this equation can be expressed in terms of the Bessel functions $J_\nu(\zeta)$ and $Y_\nu(\zeta)$ of order ν or the Hankel functions $H_\nu^{(1)}(\zeta)$ and $H_\nu^{(2)}(\zeta)$ [Abramowitz & Stegun (1970), chapter 9; hereafter this reference will be abbreviated to A&S].

Since ζ is a function of $|z|^{1-\alpha}\omega$, it follows from eq. (3) that $P(z, \omega)$ obeys the similarity property

$$P(\beta z, \omega) \propto P(z, \beta^{1-\alpha}\omega), \tag{8}$$

for $\beta > 0$. (We use the proportionality symbol '$\propto$' rather than the equality symbol '=' because when Q is multiplied by an arbitrary function of ω, P still obeys the wave equation but is no longer a function of ζ alone.)

The Bessel and Hankel functions can be seen as special cases of the Whittaker functions treated by Brekhovskikh & Godin (1990). These authors use these functions to derive reflection coefficients for a homogeneous upper half-space and a large variety of 1-D inhomogeneous lower half-spaces. However, they do not treat configurations in which the velocity function is singular, as we will do below.

THE SELF-SIMILAR INTERFACE

From here onward we consider a self-similar singularity, embedded between two homogeneous half-spaces. The depth-dependent

propagation velocity is

$$c(z)=\begin{cases} c_1 & \text{for } z\le z_1 \\ c_1|z/z_1|^{\alpha} & \text{for } z_1<z<0 \\ c_2|z/z_2|^{\alpha} & \text{for } 0<z<z_2 \\ c_2 & \text{for } z_2\le z\,. \end{cases} \tag{9}$$

Since the basic solutions have been derived for constant density, we can only arrive at exact reflection and transmission coefficients when we take a step function for the mass density,

$$\rho(z)=\begin{cases} \rho_1 & \text{for } z<0 \\ \rho_2 & \text{for } z>0\,. \end{cases} \tag{10}$$

In the following sections we derive the scattering properties of the embedded singularity, described by eqs (9) and (10). We will use the solutions of the previous section in the self-similar regions $z_1<z<0$ and $0<z<z_2$. The limits for $|z|\to 0$ of these solutions and their derivatives exist when $\alpha<1/2$. Under this condition the singular point causes no problems and we will simply connect the solutions in both regions by assuming continuity of $P(z,\omega)$ and $V(z,\omega)$ at the singular point $z=0$. Here $V(z,\omega)$ denotes the vertical component of the particle velocity, with $-j\omega\rho V=\partial P/\partial z$.

PROPAGATION MATRICES

In this section we omit the variable ω for notational convenience. We introduce propagation matrices $\mathbf{P}(z_1,z)$ and $\mathbf{P}(z,z_2)$ via

$$\begin{pmatrix} P(z_1) \\ V(z_1) \end{pmatrix}=\mathbf{P}(z_1,z)\begin{pmatrix} P(z) \\ V(z) \end{pmatrix}, \tag{11}$$

for $z_1<z<0$ ('region 1'), and

$$\begin{pmatrix} P(z) \\ V(z) \end{pmatrix}=\mathbf{P}(z,z_2)\begin{pmatrix} P(z_2) \\ V(z_2) \end{pmatrix}, \tag{12}$$

for $0<z<z_2$ ('region 2'). Since these expressions should hold for any $P(z)$ and $V(z)$ that obey the wave equation, we obtain

$$\mathbf{P}(z_1,z)=\mathbf{J}_1(z_1)\mathbf{J}_1^{-1}(z), \tag{13}$$

$$\mathbf{P}(z,z_2)=\mathbf{J}_2(z)\mathbf{J}_2^{-1}(z_2), \tag{14}$$

with

$$\mathbf{J}_n(z)=\begin{pmatrix} P_n^{(1)}(z) & P_n^{(2)}(z) \\ V_n^{(1)}(z) & V_n^{(2)}(z) \end{pmatrix}, \tag{15}$$

where $P_n^{(1)}(z)$ and $P_n^{(2)}(z)$ are arbitrary linearly independent solutions of the wave equation in region n (for $n=1$ and $n=2$), and $V_n^{(1)}(z)$ and $V_n^{(2)}(z)$ are the corresponding particle velocities. For later convenience we choose 'downgoing' and 'upgoing' waves for $P_n^{(1)}(z)$ and $P_n^{(2)}(z)$, respectively, according to

$$\mathbf{J}_n(z)=\begin{pmatrix} U_n(z) & U_n^*(z) \\ W_n(z) & -W_n^*(z) \end{pmatrix}, \tag{16}$$

where * denotes complex conjugation, and

$$U_n(z)=\zeta_n^{\nu}H_{\nu}^{(n)}(\zeta_n), \tag{17}$$

$$W_n(z)=\frac{-1}{j\omega\rho_n}\frac{\partial U_n(z)}{\partial z}=s_n j\frac{|z/z_n|^{-\alpha}}{\rho_n c_n}\zeta_n^{\nu}\left[H_{\nu+1}^{(n)}(\zeta_n)-\frac{2\nu}{\zeta_n}H_{\nu}^{(n)}(\zeta_n)\right], \tag{18}$$

with $s_1=1$, $s_2=-1$, $\zeta_n=\chi_n|z/z_n|^{1/2\nu}$, $\nu=(2-2\alpha)^{-1}$ and $\chi_n=2\nu\omega|z_n|/c_n$.

Assuming continuity of $P(z)$ and $V(z)$ at the singular point $z=0$, we obtain from eqs (11) and (12)

$$\begin{pmatrix} P(z_1) \\ V(z_1) \end{pmatrix}=\mathbf{P}(z_1,0^-)\mathbf{P}(0^+,z_2)\begin{pmatrix} P(z_2) \\ V(z_2) \end{pmatrix}, \tag{19}$$

where

$$\mathbf{P}(z_1,0^-)=\lim_{z\uparrow 0}[\mathbf{J}_1(z_1)\mathbf{J}_1^{-1}(z)], \tag{20}$$

$$\mathbf{P}(0^+,z_2)=\lim_{z\downarrow 0}[\mathbf{J}_2(z)\mathbf{J}_2^{-1}(z_2)]. \tag{21}$$

According to eq. (16) these limits are defined in terms of the limits of $U_n(z)$ and $W_n(z)$. Using A&S eqs (9.1.3), (9.1.10), (6.1.15) and (6.1.17), we obtain, for $|z|\to 0$,

$$U_n(z)\to -s_n j\frac{2^{\nu}\Gamma(\nu)}{\pi}, \tag{22}$$

$$W_n(z)\to\frac{2\chi_n^{2\nu-1}\,\mathrm{e}^{-js_n\nu\pi}\Gamma(1-\nu)}{\rho_n c_n 2^{\nu}\pi}, \tag{23}$$

under the condition that $\alpha<1/2$.

For large ζ_n (i.e. large $|z|$ and/or large ω) we obtain [using A&S eq. (9.2.3)]

$$U_n(z)\to\sqrt{\frac{2}{\pi}}\zeta_n^{\nu-1/2}\exp\left[s_n j\left(\zeta_n-\frac{\nu\pi}{2}-\frac{\pi}{4}\right)\right], \tag{24}$$

$$W_n(z)\to\frac{|z/z_n|^{-\alpha}}{\rho_n c_n}U_n(z). \tag{25}$$

ENERGY CONSERVATION

From the results in the previous section, as well as A&S eqs (6.1.17) and (9.1.17), $\det[\mathbf{P}(z_1,0^-)]=\det[\mathbf{P}(0^+,z_2)]=1$. Furthermore, owing to the structure of eq. (16), the diagonal elements in $\mathbf{P}(z_1,0^-)$ and $\mathbf{P}(0^+,z_2)$ are real whereas their off-diagonal elements are imaginary. Using eq. (19) we obtain

$$P(z_1)V^*(z_1)+P^*(z_1)V(z_1)=P(z_2)V^*(z_2)+P^*(z_2)V(z_2), \tag{26}$$

which expresses conservation of energy.

DECOMPOSITION AND COMPOSITION MATRICES

At the boundaries z_1 and z_2 of the self-similar region we introduce a decomposition matrix $\mathbf{L}^{-1}(z_1)$ and a composition matrix $\mathbf{L}(z_2)$ via

$$\begin{pmatrix} P^+(z_1) \\ P^-(z_1) \end{pmatrix}=\mathbf{L}^{-1}(z_1)\begin{pmatrix} P(z_1) \\ V(z_1) \end{pmatrix} \tag{27}$$

and

$$\begin{pmatrix} P(z_2) \\ V(z_2) \end{pmatrix}=\mathbf{L}(z_2)\begin{pmatrix} P^+(z_2) \\ P^-(z_2) \end{pmatrix}, \tag{28}$$

where $P^+(z)$ and $P^-(z)$ represent downgoing and upgoing waves, respectively. Using flux normalization (Frasier 1970; Ursin 1983), we obtain

$$\mathbf{L}(z_n) = \frac{1}{\sqrt{2}} \begin{pmatrix} (\rho_n c_n)^{1/2} & (\rho_n c_n)^{1/2} \\ (\rho_n c_n)^{-1/2} & -(\rho_n c_n)^{-1/2} \end{pmatrix}. \tag{29}$$

From eqs (26)–(29) we find, for the flux-normalized downgoing and upgoing waves,

$$P^+(z_1)[P^+(z_1)]^* - P^-(z_1)[P^-(z_1)]^* = P^+(z_2)[P^+(z_2)]^* - P^-(z_2)[P^-(z_2)]^*. \tag{30}$$

Combining eqs (19), (27) and (28) yields

$$\begin{pmatrix} P^+(z_1) \\ P^-(z_1) \end{pmatrix} = \mathbf{X}(z_1, z_2) \begin{pmatrix} P^+(z_2) \\ P^-(z_2) \end{pmatrix}, \tag{31}$$

where the transfer matrix $\mathbf{X}(z_1, z_2)$ is

$$\mathbf{X}(z_1, z_2) = \mathbf{L}^{-1}(z_1)\mathbf{P}(z_1, 0^-)\mathbf{P}(0^+, z_2)\mathbf{L}(z_2). \tag{32}$$

Note that $\det[\mathbf{L}(z_1)] = \det[\mathbf{L}(z_2)] = -1$ and hence $\det[\mathbf{X}(z_1, z_2)] = 1$.

REFLECTION AND TRANSMISSION COEFFICIENTS

We introduce reflection and transmission coefficients R^+ and T^+ for a downgoing incident field at z_1 via

$$\begin{pmatrix} 1 \\ R^+ \end{pmatrix} = \mathbf{X}(z_1, z_2) \begin{pmatrix} T^+ \\ 0 \end{pmatrix}, \tag{33}$$

where, analogously to eq. (30),

$$1 - |R^+|^2 = |T^+|^2. \tag{34}$$

Combining eq. (33) with a similar equation for the reflection and transmission coefficients R^- and T^- for an upgoing incident field at z_2 yields

$$\begin{pmatrix} 1 & 0 \\ R^+ & T^- \end{pmatrix} = \mathbf{X}(z_1, z_2) \begin{pmatrix} T^+ & R^- \\ 0 & 1 \end{pmatrix}, \tag{35}$$

with

$$1 - |R^-|^2 = |T^-|^2. \tag{36}$$

From eq. (35) we obtain

$$\begin{pmatrix} 1/T^+ & -R^-/T^+ \\ R^+/T^+ & -R^+R^-/T^+ + T^- \end{pmatrix} = \begin{pmatrix} X_{11} & X_{12} \\ X_{21} & X_{22} \end{pmatrix}, \tag{37}$$

where X_{11}, X_{12}, X_{21} and X_{22} are the elements of matrix $\mathbf{X}(z_1, z_2)$, defined in eq. (32). Hence,

$$R^+ = X_{21}/X_{11}, \tag{38}$$

$$R^- = -X_{12}/X_{11}, \tag{39}$$

$$T^+ = 1/X_{11}, \tag{40}$$

$$T^- = (X_{11}X_{22} - X_{21}X_{12})/X_{11} = T^+. \tag{41}$$

EXAMPLE 1: EXACT REFLECTION AND TRANSMISSION RESPONSES

We consider a self-similar interface, for which the velocity function is described by eq. (9), with α, c_n and z_n defined in Table 1 (Fig. 3a); the density is taken constant throughout the examples and will for convenience be set to unity. With these values the expressions (38)–(41) yield the reflection and transmission coefficients for this specific interface. For display purposes, we apply a traveltime correction, according to

$$R^+ \to \mathrm{e}^{2j\omega\tau_1} R^+, \tag{42}$$

$$R^- \to \mathrm{e}^{2j\omega\tau_2} R^-, \tag{43}$$

$$T^\pm \to \mathrm{e}^{j\omega(\tau_1+\tau_2)} T^\pm, \tag{44}$$

where τ_n is defined as the 'primary traveltime' in region n (for $n = 1$ and $n = 2$), according to

$$\tau_n = \frac{1}{c_n} \int_0^{|z_n|} \left| \frac{z}{z_n} \right|^{-\alpha} dz = \frac{1}{1-\alpha} \frac{|z_n|}{c_n} = \chi_n/\omega. \tag{45}$$

In Fig. 5 the modulus and phase of R^+ and T^+ are shown as a function of the frequency $f = \omega/2\pi$. The low- and high-frequency limits will be derived in the next two sections.

Next we consider the time-domain reflection and transmission reponses of the same interface. For the downgoing incident wavefield at $z_1 = -5$ m we choose a Ricker wavelet, defined by $s_R(t) = (1 - 2\pi^2 f_0^2 t^2)\,\mathrm{e}^{-\pi^2 f_0^2 t^2}$, with $f_0 = 50$ Hz (Fig. 6). Multiplying the spectrum of this wavelet $S_R(f) = (2/\sqrt{\pi})(f^2/f_0^3)\,\mathrm{e}^{-f^2/f_0^2}$ by the complex reflection and transmission coefficients of Fig. 5 (but without traveltime correction) and transforming the results back to the time domain yields the reflection and transmission responses at $z_1 = -5$ m and $z_2 = 5$ m. The results are shown in Figs 7(a) and (b), respectively. Note that the reflection response is shifted in time with respect to the incident wavefield by an amount of approximately $2\tau_1 = 8.9$ ms as a result of propagation to and from the singular point. Moreover, a significant phase distortion is observed, in agreement with Fig. 5(b). The transmission response, which is shifted by approximately $\tau_1 + \tau_2 = 7.4$ ms, has undergone nearly no phase distortion, in agreement with Fig. 5(d).

ZERO-FREQUENCY LIMIT

The reflection and transmission coefficients $R^\pm$ and $T^\pm$ as $\omega \to 0$ are found by substituting identity matrices for the propagation matrices $\mathbf{P}(z_1, 0^-)$ and $\mathbf{P}(0^+, z_2)$, so that the transfer matrix $\mathbf{X}(z_1, z_2)$ reduces to

$$\mathbf{X}(z_1, z_2) = \mathbf{L}^{-1}(z_1)\mathbf{L}(z_2). \tag{46}$$

From eqs (29) and (38)–(41) we obtain

$$R^+ = -R^- \to \frac{\rho_2 c_2 - \rho_1 c_1}{\rho_2 c_2 + \rho_1 c_1}, \tag{47}$$

$$T^+ = T^- \to \frac{2\sqrt{\rho_2 c_2 \rho_1 c_1}}{\rho_2 c_2 + \rho_1 c_1} = \sqrt{1 - (R^+)^2}. \tag{48}$$

These coefficients are equal to the flux-normalized coefficients for a discrete boundary between two homogeneous half-spaces, where the velocity and density are described by step functions. This is consistent with the multiscale analysis in Fig. 3, which revealed that for large σ the embedded self-similar singularity behaves as a step function (the scale σ is proportional to the wavelength, so $\sigma \to \infty$ corresponds to $\omega \to 0$). For the values of c_n in Table 1 (and $\rho_1 = \rho_2$), eqs (47) and (48) yield $R^+ = -R^- \to 0.2$ and $T^\pm \to \sqrt{0.96}$ (see Figs 5a and c for $f \to 0$).

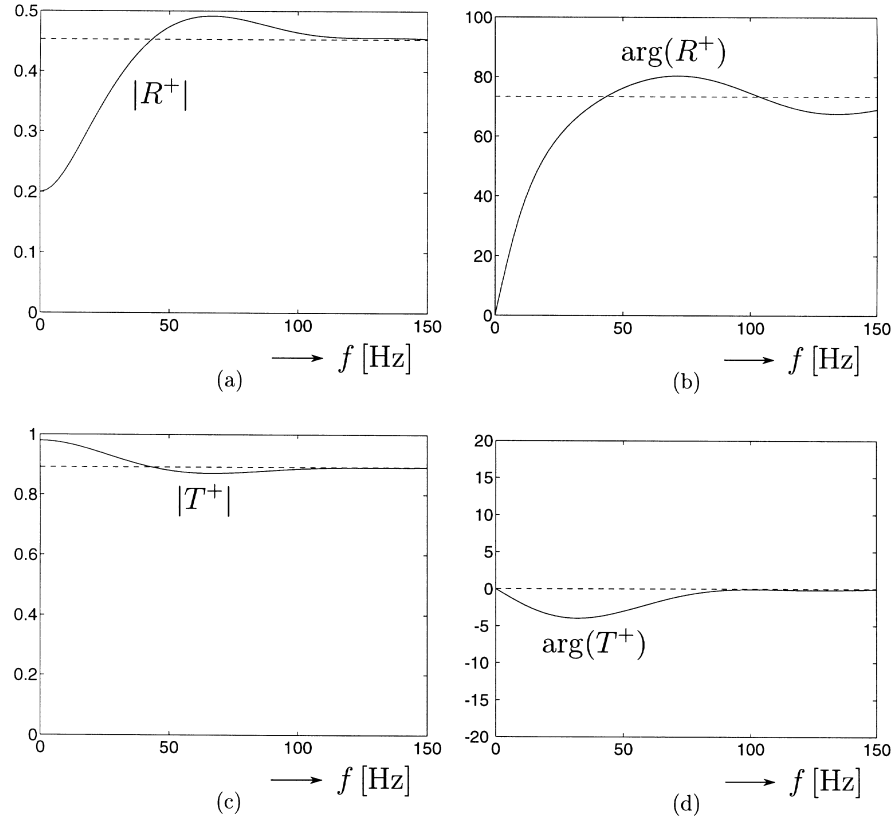

Figure 5. Modulus and phase as a function of frequency of the reflection coefficient R^+ (a, b) and of the transmission coefficient T^+ (c, d) of the embedded singularity of Fig. 3(a). The solid lines are the exact coefficients and the dashed lines are their high-frequency approximations.

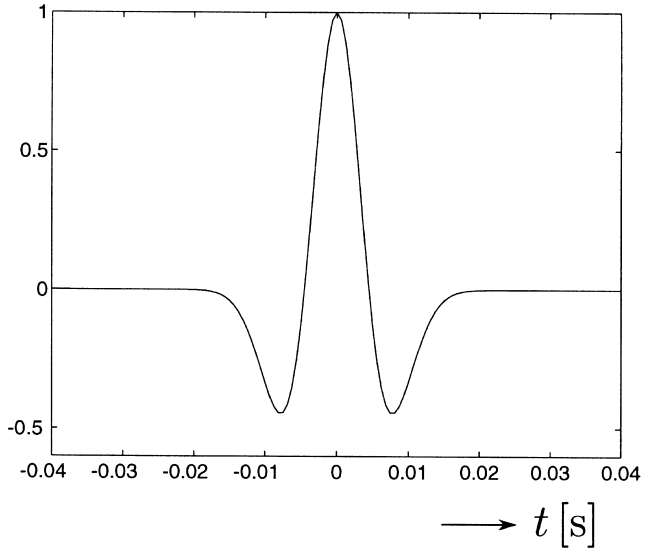

Figure 6. Incident downgoing wavefield (Ricker wavelet with central frequency $f_0 = 50$ Hz) at $z_1 = -5$ m (i.e. the upper boundary of the embedded singularity of Fig. 3a). The responses in Figs 7, 10 and 12 are plotted with the same amplitude scaling.

HIGH-FREQUENCY BEHAVIOUR

The high-frequency behaviour of the scattering coefficients may be analysed, using the asymptotic expressions (24) and (25). In this section we take $|z_1| = |z_2|$.

For this high-frequency analysis it is convenient to regroup the matrices that contribute to the transfer matrix

$$\begin{aligned}\mathbf{X}(z_1, z_2) &= \mathbf{L}^{-1}(z_1)\mathbf{J}_1(z_1)\mathbf{J}_1^{-1}(0^-)\mathbf{J}_2(0^+)\mathbf{J}_2^{-1}(z_2)\mathbf{L}(z_2)\\ &= \mathbf{A}_1\mathbf{B}\mathbf{A}_2^{-1},\end{aligned} \tag{49}$$

where

$$\mathbf{A}_n = \mathbf{L}^{-1}(z_n)\mathbf{J}_n(z_n), \tag{50}$$

$$\mathbf{B} = \mathbf{J}_1^{-1}(0^-)\mathbf{J}_2(0^+). \tag{51}$$

Matrices $\mathbf{A}_n$ and $\mathbf{B}$ will be separately analysed. Using eqs (16), (25) and (29), we obtain, for the high-frequency behaviour of $\mathbf{A}_n$,

$$\begin{aligned}\mathbf{A}_n \rightarrow &\frac{1}{\sqrt{2}}\begin{pmatrix}(\rho_n c_n)^{-1/2} & (\rho_n c_n)^{1/2}\\ (\rho_n c_n)^{-1/2} & -(\rho_n c_n)^{1/2}\end{pmatrix}\\ &\times\begin{pmatrix}U_n(z_n) & U_n^*(z_n)\\ U_n(z_n)/\rho_n c_n & -U_n^*(z_n)/\rho_n c_n\end{pmatrix}\\ &= \sqrt{\frac{2}{\rho_n c_n}}\begin{pmatrix}U_n(z_n) & 0\\ 0 & U_n^*(z_n)\end{pmatrix}.\end{aligned} \tag{52}$$

Substituting this result in eq. (49) yields

$$\begin{aligned}&\begin{pmatrix}X_{11} & X_{12}\\ X_{21} & X_{22}\end{pmatrix}\\ &\rightarrow \sqrt{\frac{\rho_2 c_2}{\rho_1 c_1}}\begin{pmatrix}[U_1(z_1)/U_2(z_2)]B_{11} & [U_1(z_1)/U_2^*(z_2)]B_{12}\\ [U_1^*(z_1)/U_2(z_2)]B_{21} & [U_1^*(z_1)/U_2^*(z_2)]B_{22}\end{pmatrix},\end{aligned} \tag{53}$$

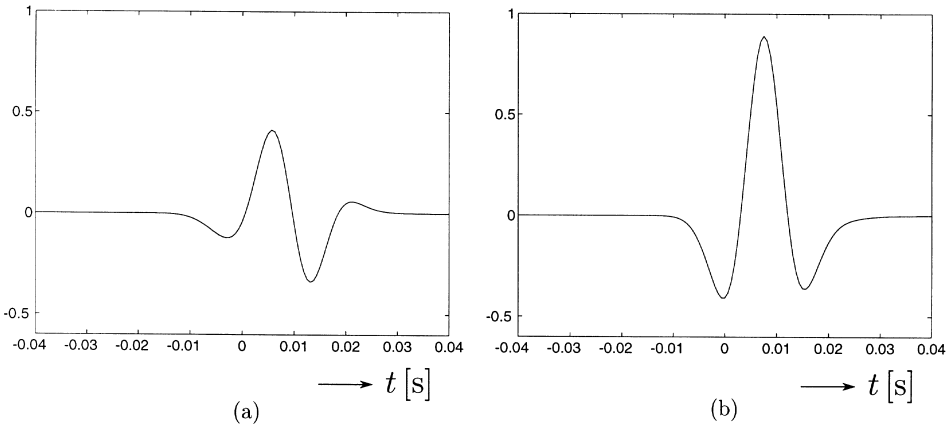

Figure 7. (a) Reflected upgoing wavefield at $z_1 = -5$ m (the upper boundary of the embedded singularity of Fig. 3a). (b) Transmitted downgoing wavefield at $z_2 = 5$ m (the lower boundary of the embedded singularity of Fig 3a).

where B_{11}, B_{12}, B_{21} and B_{22} are the elements of matrix **B**, defined in eq. (51). From eqs (16), (22) and (23) we find

$$B_{11} = \frac{-e^{jv\pi}}{2j\sin(v\pi)}\left(1 + \frac{\rho_1 c_1^{2v}}{\rho_2 c_2^{2v}}\right), \tag{54}$$

$$B_{21} = \frac{-1}{2j\sin(v\pi)}\left(e^{-jv\pi} + e^{jv\pi}\frac{\rho_1 c_1^{2v}}{\rho_2 c_2^{2v}}\right), \tag{55}$$

$$B_{12} = B_{21}^*, \tag{56}$$

$$B_{22} = B_{11}^*. \tag{57}$$

Using eqs (24) and (38)–(41) yields the asymptotic expressions for the reflection and transmission coefficients,

$$R^+ = \frac{X_{21}}{X_{11}} \rightarrow \frac{U_1^*(z_1)}{U_1(z_1)}\frac{B_{21}}{B_{11}}$$
$$= je^{-2j\chi_1}\left(\frac{e^{-jv\pi}\rho_2 c_2^{2v} + e^{jv\pi}\rho_1 c_1^{2v}}{\rho_2 c_2^{2v} + \rho_1 c_1^{2v}}\right), \tag{58}$$

$$R^- = -\frac{X_{12}}{X_{11}} \rightarrow -\frac{U_2(z_2)}{U_2^*(z_2)}\frac{B_{12}}{B_{11}}$$
$$= je^{-2j\chi_2}\left(\frac{e^{jv\pi}\rho_2 c_2^{2v} + e^{-jv\pi}\rho_1 c_1^{2v}}{\rho_2 c_2^{2v} + \rho_1 c_1^{2v}}\right), \tag{59}$$

$$T^{\pm} = \frac{1}{X_{11}} \rightarrow \sqrt{\frac{\rho_1 c_1}{\rho_2 c_2}}\frac{U_2(z_2)}{U_1(z_1)}\frac{1}{B_{11}}$$
$$= 2e^{-j(\chi_1+\chi_2)}\sin(v\pi)\left(\frac{\sqrt{\rho_2 c_2^{2v}\rho_1 c_1^{2v}}}{\rho_2 c_2^{2v} + \rho_1 c_1^{2v}}\right). \tag{60}$$

Note that the exponentials containing χ_n account for the primary traveltimes in region n, see eq. (45). If we apply a traveltime correction according to eqs (42), (43) and (44), the coefficients in eqs (58), (59) and (60) become frequency-independent. These coefficients are equal to those for a self-similar function described by eq. (1) [i.e. without the embedding homogeneous half-spaces, see Wapenaar (1998)]. This is consistent with the multiscale analysis in Fig. 3, which revealed that for small σ the embedding half-spaces have no effect on the scaling behaviour of the singularity, as can be confirmed in Fig. 8 (bear in mind that $\sigma \rightarrow 0$ corresponds to $\omega \rightarrow \infty$). At this point it is useful to give a quantitative interpretation of the scales σ

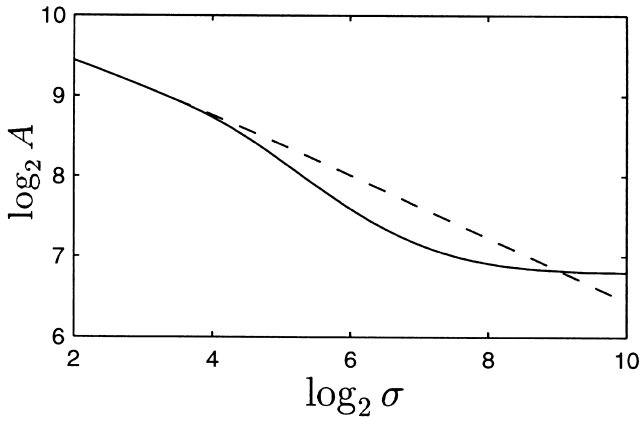

Figure 8. Comparison of the AVS curves of Figs 3(d) (solid) and 2(d) (dashed). For small scales they are indistinguishable.

along the horizontal axes in these figures. As mentioned in the introduction, the multiscale analysis involves a convolution with a scaled wavelet $(1/\sigma)\psi(z/\sigma)$. The wavelet that was used in Figs 2–4 is the derivative of a Gaussian, defined as

$$\psi\left(\frac{z}{\sigma}\right) = \frac{\partial}{\partial z}\left(\frac{\exp[-(z/2\sigma\Delta z)^2]}{2\sqrt{\pi}}\right), \tag{61}$$

with $\Delta z = 0.1$ m. The Fourier transform of this wavelet is $j(k\sigma\Delta z)\exp[-(k\sigma\Delta z)^2]$ and reaches its maximum at $k_0 = 1/(\sigma\Delta z\sqrt{2})$. Hence, the effective wavelength of the analysing wavelet is given by $\lambda_{\text{eff}} = 2\pi/k_0 = 2\sqrt{2}\pi\sigma\Delta z$, from which we derive that $\log_2\sigma = \{2, 4, 6, 8, 10\}$ corresponds to $\lambda_{\text{eff}} = \{3.5, 14, 57, 228, 910\}$ m. Unfortunately these wavelengths cannot be uniquely related to seismic frequencies, since the velocity is not constant. Using an effective velocity c_{eff} we define the corresponding effective seismic frequency as $f_{\text{eff}} = c_{\text{eff}}/\lambda_{\text{eff}}$. Choosing (quite arbitrarily) $c_{\text{eff}} = 2000$ m s^{-1}, we thus find that the aforementioned range of scales corresponds to $f_{\text{eff}} = \{570, 142, 34, 9, 2.2\}$ Hz. Hence, the scales $\log_2\sigma = 4$ to $\log_2\sigma = 8$ roughly correspond to the seismic frequency range. In Fig. 8 we observe that the AVS curves of the velocity functions in Figs 2 and 3 match very accurately for scales smaller than the seismic scales; within the seismic frequency range they follow a similar trend and for larger scales they

are completely different. Hence, the high-frequency approximations derived in this section are very accurate for frequencies above the seismic frequency range. How well they perform within the seismic frequency range will be investigated with an example.

EXAMPLE 2: ASYMPTOTIC REFLECTION AND TRANSMISSION RESPONSES

For c_n and z_n as listed in Table 1 and *variable* α, the modulus and phase of the high-frequency reflection and transmission coefficients R^+ and T^+ are shown in Figs 9(a) and (b). For $\alpha = -0.4$ we have $|R^{\pm}| \to 0.4528$, $\arg(R^+) \to 73.37°$, $\arg(R^-) \to 106.63°$, $|T^{\pm}| \to 0.8916$ and $\arg(T^{\pm}) \to 0°$. These values [except $\arg(R^-)$] are represented by the dashed lines in Fig. 5.

Multiplying these high-frequency coefficients (for $\alpha = -0.4$) by the spectrum $S_R(f)$ of the Ricker wavelet of Fig. 6 and transforming the results back to the time domain yields the asymptotic reflection and transmission responses at $z_1 = -5$ m and $z_2 = 5$ m, respectively. The results are represented by the crosses (+) in Figs 10(a) and (b), respectively; the solid lines in these figures are the exact responses of Figs 7(a) and (b). Note that the main features of the exact responses (time-shift and phase behaviour) are reasonably well reproduced by the high-frequency approximations.

THE EFFECT OF SINGULARITY SMOOTHING

In Fig. 4 in the introduction we presented a multiscale analysis of a smoothed version of an embedded singularity (as a matter of fact the smoothing was applied to the slowness in order to leave the 'primary traveltimes' unaffected, and hence the function in Fig. 4a actually represents the reciprocal of the smoothed slowness). Remember that the smoothing was introduced to change the small-scale behaviour of the singularity. A comparison of the AVS curves of the singularity before and after smoothing is shown in Fig. 11. Note that in the seismic scale range ($\log_2 \sigma = 4$ to $\log_2 \sigma = 8$) both AVS curves reveal approximately the same constant-slope behaviour. Hence, we may expect that the smoothing has not much effect on the seismic reflection and transmission responses. Since no analytical expressions are available for the reflection and transmission coefficients of a smoothed singularity, the responses will be modelled with the 'reflectivity method' (see e.g. Kennett

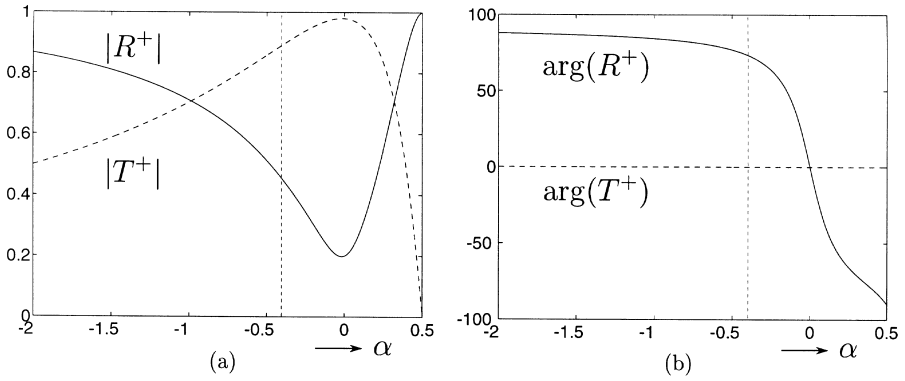

Figure 9. High-frequency approximation of the modulus (a) and phase (b) of the reflection coefficient R^+ (solid) and the transmission coefficient T^+ (dashed). The coefficients are plotted as a function of the singularity exponent α; the parameters c_n and z_n are defined in Table 1. For $\alpha = -0.4$ the moduli and phases correspond to those in Fig. 5 for $f \to \infty$.

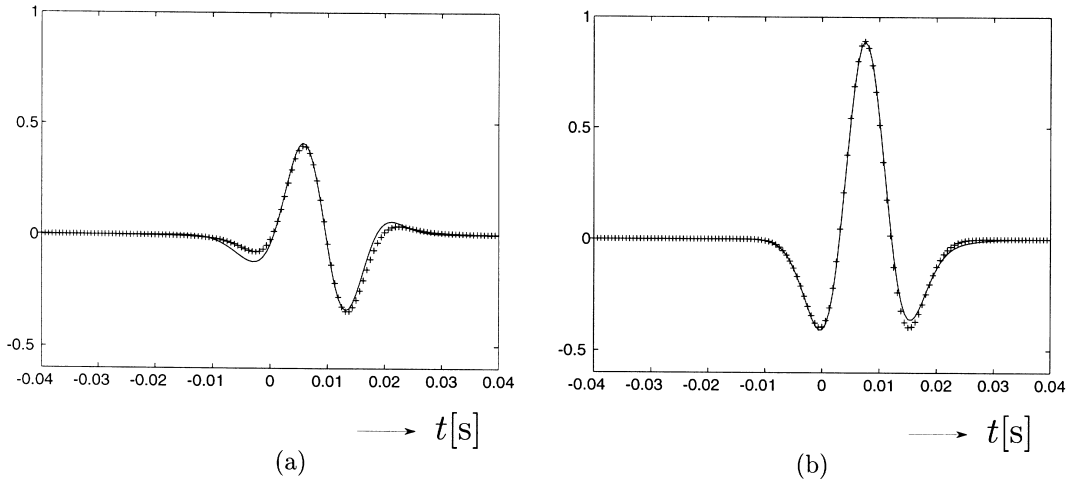

Figure 10. (a) Exact (solid line) and high-frequency approximation (+) of the reflection response of the embedded singularity of Fig. 3(a) (the incident wavefield was again the Ricker wavelet of Fig. 6). (b) As (a), for transmission response.

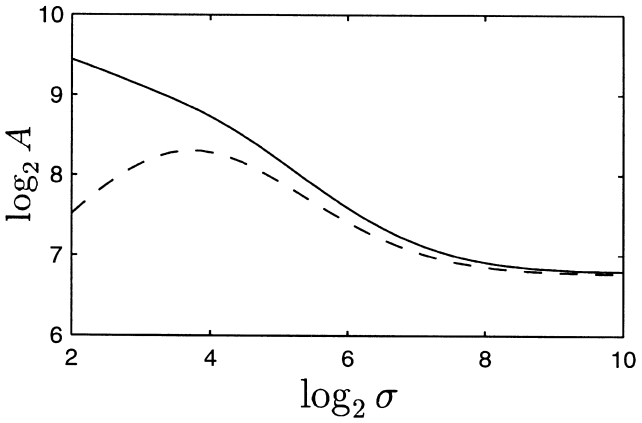

Figure 11. AVS curves of the embedded self-similar interface (solid) and its smoothed version (dashed), copied from Figs 3(d) and 4(d), respectively.

& Kerry 1979). For the incident downgoing wavefield we choose again a Ricker wavelet with a central frequency $f_0 = 50$ Hz; the layer thickness is set to $\Delta z = 1$ m. The numerically modelled reflection and transmission responses of the smoothed interface in Fig. 4(a) are represented by the crosses (+) in Figs 12(a) and (b), respectively; the solid lines in these figures are again the exact responses of the unsmoothed interface. Note that the match is very accurate. This implies that our analytical expressions are approximately valid for modelling the band-limited response of an interface of which the AVS curve has a constant slope in a finite scale range, corresponding to the seismic frequency range; the behaviour of the AVS curve at smaller scales has hardly any effect on the seismic response.

CONCLUSIONS

Outliers in well logs often behave quite differently from step-functions. Multiscale analysis (Mallat & Hwang 1992) applied to these outliers yields AVS curves that often reveal a constant-slope behaviour for a finite range of scales (Herrmann 1997). We parametrized these outliers by self-similar singularities. The AVS curves of these singularities have a constant slope for all scales (Fig. 2). To comply with realistic situations we applied two modifications to the self-similar singularity in such a way that the constant-slope behaviour of the AVS curve is preserved for a finite range of scales.

(1) We introduced a scale-dependent interface in which the self-similar singularity is embedded between two homogeneous half-spaces. A multiscale analysis (Fig. 3) revealed that for small scales ($\sigma \to 0$) the AVS curve retains its constant slope (i.e. the effect of the embedding half-spaces vanishes), whereas for large scales ($\sigma \to \infty$) this interface is indistinguishable from the usual step function. We have derived analytical expressions for the normal-incidence reflection and transmission coefficients of this interface. These coefficients appear to be frequency-dependent. For large frequencies ($\omega \to \infty$) the coefficients are equal to those of a self-similar function (i.e. without the embedding half-spaces), whereas for small frequencies ($\omega \to 0$) these coefficients reduce to the well-known coefficients of a step-function interface.

(2) We also changed the small-scale ($\sigma \to 0$) AVS behaviour of the self-similar singularity by smoothing. This was done in such a way that in the seismic scale range the constant-slope behaviour was hardly affected (Fig. 4). Using a numerical method it was shown that the reflection and transmission reponses of the smoothed embedded singularity accurately match those of the unsmoothed singularity.

Since seismic data are always band-limited, the analytical reflection and transmission coefficients derived in this paper are suited to model the response of scale-dependent interfaces of which the AVS curves reveal a constant-slope behaviour in a finite scale range that corresponds to the seismic frequency range.

Throughout this paper we have restricted ourselves to the acoustic normal-incidence response of one particular class of scale-dependent reflector models. Since the analytic results are exact, they may serve as a reference for approximate expressions for more general situations. Dessing (1997) analyses the response of another class of scale-dependent reflector models. For a symmetric self-similar singularity (without embedding half-spaces), his results are consistent with the high-frequency approximations in this paper. For the oblique-incidence response no explicit expressions have been found yet (except for $\alpha = 0$ and $\alpha = -1/2$). However, by exploiting

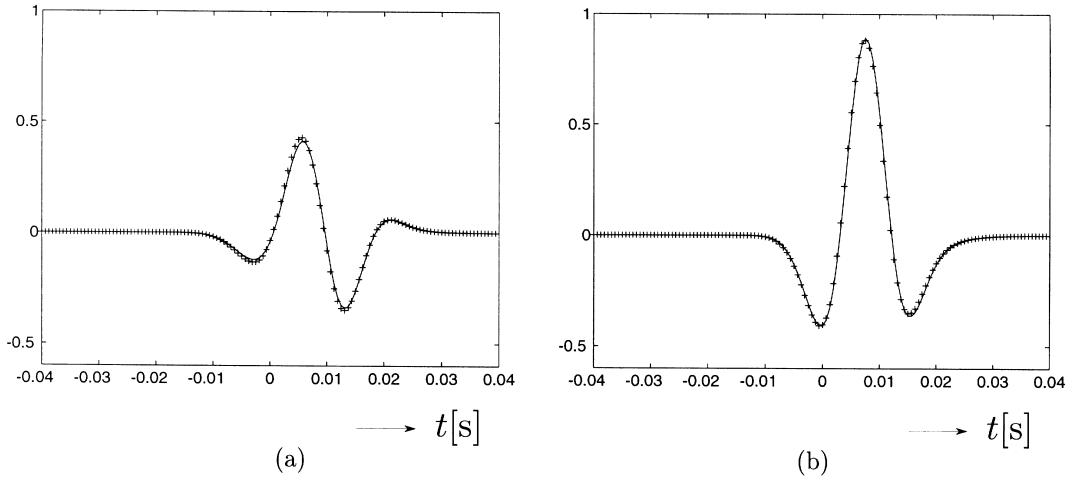

Figure 12. (a) Reflection response of the embedded singularity of Fig. 3(a) (solid line) and its smoothed version in Fig. 4(a) (+). (b) As (a), for transmission response.

the self-similarity property $c(\beta z) = \beta^{\alpha} c(z)$, it is possible to derive self-similarity relations for the angle-dependent reflection and transmission coefficients (Wapenaar 1998). A further discussion of these extensions is beyond the scope of this paper.

ACKNOWLEDGMENTS

The author would like to thank Frank Dessing and Jeroen Goudswaard for fruitful discussions and for carrying out the multiscale analyses of the singular functions. The financial support of the Dutch Technology Foundation (STW) is highly appreciated.

REFERENCES

Abramowitz, M. & Stegun, I.A., 1970. *Handbook of Mathematical Functions,* Dover, New York.

Brekhovskikh, L.M. & Godin, O.A., 1990. *Acoustics of Layered Media. Part 1. Plane and Quasi-plane Waves,* Springer, Berlin.

Dessing, F.J., 1997. A wavelet transform approach to seismic processing, *PhD thesis,* Delft University of Technology.

Frasier, C.W., 1970. Discrete time solution of plane *P–SV* waves in a plane layered medium, *Geophysics,* **35,** 197–219.

Herrmann, F.J., 1997. A scaling medium representation, *PhD thesis,* Delft University of Technology.

Herrmann, F.J. & Staal, J., 1996. Waves in scaling media; the implication of non-differentiability, *58th Meet. Eur. Assoc. Expl. Geophys.,* Abstracts, Session C007.

Kennett, B.L.N. & Kerry, N.J., 1979. Seismic waves in a stratified half-space, *Geophys. J. R. astr. Soc.,* **57,** 557–584.

Mallat, S.G. & Hwang, W.L., 1992. Singularity detection and processing with wavelets, *IEEE Trans. Inform. Theory,* **38,** 617–643.

Ursin, B., 1983. Review of elastic and electromagnetic wave propagation in horizontally layered media, *Geophysics,* **48,** 1063–1081.

Wapenaar, C.P.A., 1998. Amplitude-versus-angle behaviour of self-similar interfaces, *Geophysics,* **63,** accepted.